Mathematical modelling of Tyndall star initiation

A. A. L A C E Y[1], M. G. H E N N E S S Y[2], P. H A R V E Y[3]† and R. F. K A T Z[4]

[1]*Maxwell Institute for Mathematical Sciences and Department of Mathematics,*
School of Mathematical and Computer Sciences, Heriot-Watt University,
Edinburgh, EH14 4AS, UK
[2]*Department of Chemical Engineering, Imperial College,*
London, SW7 2AZ, UK
[3]*Department of Physics & Astronomy,University College London,*
Gower Street, London, WC1E 6BT, UK
[4]*Department of Earth Sciences, University of Oxford,*
South Parks Road, Oxford, OX1 3AN, UK
email: *A.A.Lacey@hw.ac.uk ; m.hennessy@imperial.ac.uk ; peter.harvey.11@alumni.ucl.ac.uk ;*
richard.katz@earth.ox.ac.uk

The superheating that usually occurs when a solid is melted by volumetric heating can produce irregular solid–liquid interfaces. Such interfaces can be visualised in ice, where they are sometimes known as Tyndall stars. This paper describes some of the experimental observations of Tyndall stars and a mathematical model for the early stages of their evolution. The modelling is complicated by the strong crystalline anisotropy, which results in an anisotropic kinetic undercooling at the interface; it leads to an interesting class of free boundary problems that treat the melt region as infinitesimally thin.

Key words: Free boundary problems, kinetic Wulff shapes, anisotropic kinetic undercooling, co-dimension-two problems

1 Introduction

When a single crystal of pure, transparent ice is irradiated, the partial absorption of transmitted radiation volumetrically heats the crystal, leading to internal melting and the formation of small volumes of liquid. Remarkably, these volumes of water often take on shapes that resemble six-fold symmetric flowers, stars, or snowflakes, as first documented by Tyndall [30]. The internal melt figures that Tyndall observed now bear his name and are often referred to as Tyndall stars, Tyndall figures, or liquid snowflakes. Examples of such can be found in Figure 1.

Tyndall stars are predominantly found in very pure crystals of irradiated ice. The lack of impurities and microscopic defects in such crystals limits the onset of liquid nuclei and prevents the ice from simply melting away as it continually absorbs radiation. Instead, the ice becomes superheated, whereby its temperature exceeds the equilibrium melting temperature. It is this superheating that, through an interfacial instability, is suspected

---

† The research was carried out while the author was at the Department of Earth Sciences, University of Oxford, South Parks Road, Oxford, OX1 3AN, UK.
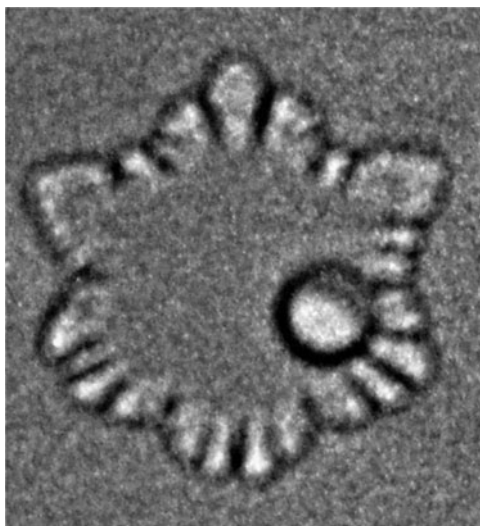
FIGURE 1. An example of a Tyndall star that has been created by irradiating a pure crystal of ice with light from a slide projector. The bright circle within the star is a vapour bubble that emerges due to the density difference between water and ice. The viewing plane corresponds to the basal plane of the melting ice crystal with the *c*-axis pointing orthogonally into and out of the page. This image was created by the authors at the FoaLab in Oxford; for additional details, see Harvey [14].

of giving rise to the complex morphologies that are characteristic of Tyndall stars. The six-fold symmetry that is apparent in Figure 1 is inherited from the anisotropy of the ice crystal, which will be discussed in detail below.

From a scientific viewpoint, Tyndall stars offer a convenient route for studying the dynamics of phase change and moving interfaces because both the solid and liquid phases are transparent. Thus, in principle, these phases can be observed in real time with visible light. Understanding of Tyndall stars may also have industrial implications in, for example, resistance welding, whereby a metal is volumetrically heated by passing an electrical current through it [2,21]. This leads to a superheated solid and the formation of small inclusions of liquid metal. Due to the opacity of the metal, these inclusions cannot be seen in real time and are often detected after the welding operation is over.

The evolution of Tyndall stars has been studied experimentally by Nakaya [24], who found that the melts begin as cylindrical discs of water with thicknesses that are much smaller than their radii. This thin aspect ratio is maintained during the evolution of a Tyndall star, with growth in the radial direction being much faster than in the axial direction. As the cylindrical disc increases in size, the circular interface can become unstable, leading to the emergence of a high-wavenumber fingering pattern. In cases where the radiation intensity was sufficiently high, further growth of the instability resulted in the formation six large symmetric dendrites. In addition, Nakaya reported that the Tyndall stars in a given ice crystal always have the same orientation. Further experiments by Takeya [29] were able to provide quantitative data for the radial and axial growth of Tyndall stars. Over the duration of a couple of minutes, the radius increased to roughly 1.5 mm while the thickness grew linearly with time to about 0.3 mm. In some
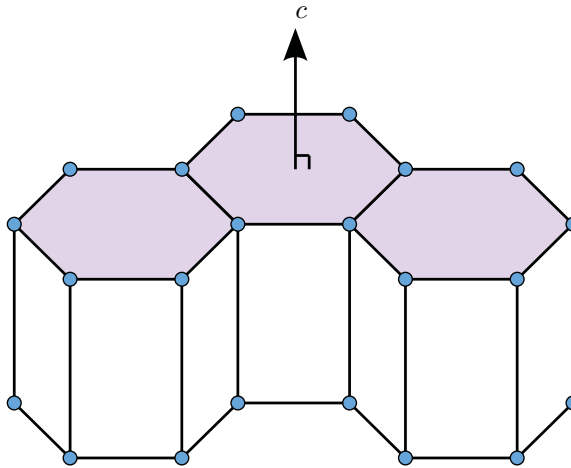
FIGURE 2. A schematic diagram of an ice crystal, which is composed of arrays of hexagonal prisms. Shaded hexagonal faces form the molecularly smooth basal planes of the ice crystal and the unshaded rectangular faces correspond to molecularly rough prism planes. The *c*-axis of the ice crystal is orthogonal to the basal planes. The shaded circles give the approximate positions of oxygen atoms. The rate of melting is much higher at prism planes than basal planes, resulting in Tyndall stars that are relatively thin in directions along the *c*-axis.

cases, however, the axial growth of the melt was only temporary and eventually it stopped altogether. Interestingly, Takeya reported that an interfacial instability only occurs when the axial growth persists; in cases where the axial growth terminates, the melt remains cylindrical.[1] This observation is perhaps linked to those made by Mae [22], who found that Tyndall stars retain their initial cylindrical shape unless they grow beyond a critical thickness of 10 μm. Experimental [28] and theoretical [37] studies of solidification in supercooled liquids, a situation that closely parallels melting into a superheated solid, have also shown that a critical thickness must be surpassed in order for a morphological instability to occur at the solid–liquid interface.

The anisotropic growth of a Tyndall star is closely related to the geometric configuration of the melting ice crystal. Roughly speaking, the crystalline structure of ice can be imagined as a collection of adjacent hexagonal prisms; see Figure 2. The hexagonal faces of the prisms form the so-called basal planes of the crystal and the direction that is normal to these planes defines the *c*-axis. The radial growth of Tyndall stars occurs within the basal planes while the axial growth is aligned with the *c*-axis, therefore giving different Tyndall stars the same orientation within an ice crystal. The molecularly smooth basal planes melt at a much slower rate than the molecularly rough prism planes. As discussed in the context of solidification [6], the accretion of material normal to a molecularly smooth surface, such as a basal plane, occurs via an energetically activated process, whereas there is no nucleation barrier at a molecularly rough surface. The fast-melting prism planes dominate the shape of the Tyndall figure [25] and are responsible for the disparity between its axial and radial dimensions.

[1] The axial growth ceased for cases of low superheating with there being sufficient heat to melt only a small part of the ice. There could be only limited scope for instability in such situations.

The mathematical study of problems involving phase change is now a classical subject for which there is extensive literature. Davis [10] gives a comprehensive treatment of the mathematical theory of solidification, starting from the classical Stefan problem. Hu & Argyropoulos [13] provide an overview of modelling and computational techniques that are relevant to solidification and melting problems. The fluid mechanics of solidification are reviewed in detail by Huppert [17]. Coriell *et al.* [8,9] examine the occurrence of multiple similarity solutions, as well as their selection mechanisms, in models of solidification and melting. The application of phase-field models to solidification problems has been discussed by Boettinger *et al.* [4].

Mathematical models of phase change that account for the anisotropic nature of the solid have been largely confined to the case of solidification and crystallisation. Wettlaufer *et al.* [6, 23, 31, 33] examined two-dimensional crystallisation within the basal plane by considering an interfacial velocity that depends on the angle between the free boundary and a certain fixed direction. A suitable angular dependence was found to give rise to the six-fold symmetry that is characteristic of snowflakes. It is important to emphasise that in the studies of Wettlaufer *et al.*, it is assumed that growth of the crystal is in the geometric limit, whereby the interface velocity is only a function of the shape and position of the interface. In particular, the velocity of the interface does not depend on field variables that are affected by its motion. This is in contrast to non-geometric growth models, which account for long-range diffusion of field variables and their coupling to the interfacial velocity. In geometric models, the crystalline anisotropy enters directly through the interface velocity. However, in non-geometric models, anisotropy enters through physical parameters related to the interface, such as surface energy or the coefficient of kinetic undercooling, the latter of which connects the temperature and velocity at the interface. Anisotropic solidification outside of the geometric limit has been investigated by a number of authors. Uehara & Sekerka [32] studied the formation of facets due to strong anisotropy in the kinetic coefficient using a phase-field model. Particular attention was paid to determining the relationship between the shape of the emerging crystal and the mathematical properties of the anisotropic kinetic coefficient. Yokoyama & Kuroda [35] employed the boundary-element method to study the hexagonal morphologies of snow crystals predicted by a model with an anisotropic kinetic coefficient. Yokoyama & Sekerka [36] explored the combined effects of anisotropic kinetic undercooling and surface energy. Using numerical and asymptotic methods, they investigated the suppression of corner formation between adjacent facets.

Considerable attention has focused for many years on the stability of the free boundary in phase-change models. Linear stability analyses of models which treat the phase interface as infinitesimally thin, such as in the pioneering study by Mullins & Sekerka [26] or in Hele–Shaw and Muskat problems, indicate that a morphological instability can arise when a melting boundary is driven by heat flow from a superheated solid region [20]. In fact, without a regularising mechanism such as surface energy or kinetic undercooling, the system is severely unstable and the model becomes ill-posed in the sense that disturbances with arbitrarily large wavenumbers will grow arbitrarily fast in time. Such ill-posedness can also be avoided by replacing the sharp, infinitesimally thin interface with a diffuse mushy region consisting of two co-existing phases [2, 20]. The theory of mushy regions in volumetrically heated solids has been developed by Lacey *et al.* [18, 19, 21], who treated the

mush as a collection of small liquid inclusions that grow within the solid. In these papers, the growth of the inclusions is modelled using classical Stefan problems that account for surface-energy effects and interfacial curvature, kinetic undercooling, and/or composition in the case of alloys. The main purpose of those studies was to use homogenisation to build an averaged model for the mushy region.

A sharp-interface model of Tyndall stars has been formulated and studied by Hennessy [15]. The focus here was on two-dimensional evolution within the basal plane. The morphology of the solid–liquid interface was studied using a combination of linear stability theory and numerical simulations. Growth along the *c*-axis was not considered and thus it was not possible to explore how this may influence the stability of the ice–water interface.

In this paper, we consider the three-dimensional evolution of a Tyndall star or, perhaps more accurately, a Tyndall figure, as we mostly discuss the earlier growth rather than the later, star-like stage. Particular attention is paid to capturing the anisotropic growth along the radial and axial directions. Our description of the problem is based on the classical Stefan model but the inclusion of volumetric heating and anisotropic kinetic undercooling makes it non-standard. An asymptotic analysis that exploits the axial and radial length-scale separation is used to reduce the three-dimensional problem to a co-dimension-2 free boundary problem whereby the melt is collapsed into a planar surface with infinitesimal thickness. A local stability analysis of the reduced model is carried out as a first step towards the study of the onset of fingering patterns at the ice–water interface. An attempt is made to compare our theoretical results to the experimental observations of Takeya [29]; however, this is not straightforward due to a lack of knowledge of key quantities controlling the anisotropic growth. We then propose future experiments that could produce novel quantitative insights into the growth kinetics.

In the next section, we present a mathematical model for a growing Tyndall figure based on laboratory experiments. In Section 3, we carry out an asymptotic analysis of this model that captures the anisotropic growth of the melt and investigates the stability of the ice–water interface. We discuss our results and conclude the paper in Section 4.

2 Mathematical model

2.1 The physical problem

We suppose that a single crystal of ice held at its melting temperature is illuminated at time $t = 0$. The direction of the incident light is taken to be parallel to the *c*-axis of the crystal; see Figure 3. We assume that a rapid nucleation process occurs within the ice upon exposure to light, leading to the creation of a single spherical melt figure. Continued absorption of radiation by both the ice and the water will drive the melting at the interface, which we aim to describe mathematically. Our model of this physical scenario is based on equations governing the temperatures in the liquid and solid phases, taking into account thermal diffusion and volumetric heat generation due to absorption of radiation. The solid–liquid interface is assumed to be sharp and, therefore, we impose appropriate boundary conditions on it.
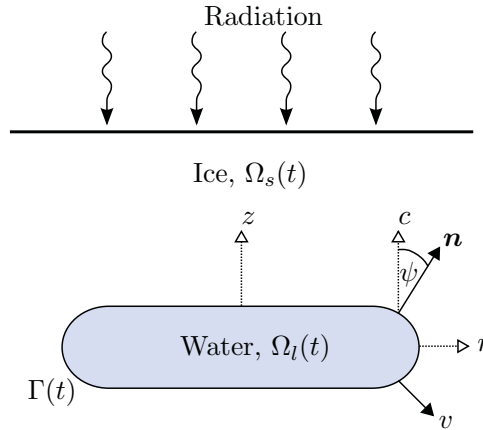
FIGURE 3. We study the growth of a Tyndall figure (depicted by the shaded region) in superheated irradiated ice. We use Ω_l and Ω_s to denote regions of space occupied by liquid water and solid ice, respectively. Here, t represents time. The ice–water interface is denoted by $\Gamma(t)$ and has a normal vector $\boldsymbol{n}$ and normal component of velocity v. The z-axis is parallel to the c-axis of the ice crystal and $r = (x^2 + y^2)^{1/2}$ is a radial coordinate that lies within the basal plane. The angle between the c-axis and the normal vector $\boldsymbol{n}$ is given by ψ.

The field equation for the temperature T_j of phase j is given by

$$\rho_j c_{pj} \frac{\partial T_j}{\partial t} = k_j \nabla^2 T_j + q_j, \quad \boldsymbol{x} \in \Omega_j(t), \tag{2.1}$$

where t is time, position is $\boldsymbol{x} = (x, y, z)$, and $\Omega_j(t)$ is the region of space occupied by phase j. We let $j = l$ and $j = s$ for the liquid water and solid ice phases, respectively. We assume that the z-axis and the (x, y) plane are aligned with the c-axis and basal planes of the ice crystal, respectively. The values of the material constants, namely the densities, ρ_j, specific heat capacities, c_{pj}, and thermal conductivities, k_j, differ between the two phases. Although the difference in density between the phases is significant enough to give rise to a vapour bubble inside the Tyndall figure, as shown in Figure 1, their relative difference is small and we take the densities of the two phases to be the same and equal to ρ, that is, $\rho_l = \rho_s = \rho$. The rates of volumetric heating, q_j, are given by the product of an absorption coefficient, μ_j, and the local intensity of incident light upon the medium, I. With a sufficiently small piece of ice (or absorption coefficient), I can be regarded as constant, making q_j constant in each phase. We shall generally assume that the initial temperatures coincide with the equilibrium melting temperature T_0 at $t = 0$, with a spherical Tyndall figure of radius a nucleating at the same instant. However, if significant body heating occurs before nucleation, the initial temperatures will be much greater than T_0. This situation is discussed in Appendix B.

At the evolving interface $\Gamma = \Gamma(t)$ between ice and water, we have the usual Stefan condition

$$L\rho v = \left[k_j \frac{\partial T_j}{\partial n} \right]_l^s, \quad \boldsymbol{x} \in \Gamma(t), \tag{2.2}$$

where L is the latent heat of fusion, assumed constant; v is the normal velocity, measured

towards the ice; $\partial/\partial n$ is the normal derivative, again in the direction into the ice; and $[\cdot]_l^s$ denotes the change in a quantity across the interface, going from liquid water to solid ice, see Figure 3.

We also assume that the normal velocity of the interface is proportional to the local amount of superheating [10]. To account for the different melting rates of the basal and prism planes, we take the constant of proportionality to be a function of the orientation of the interface. Thus, we impose a kinetic condition, equivalent to anisotropic kinetic undercooling in solidification [32, 35, 36], given by

$$v = K f(\psi)(T_I - T_0), \quad \boldsymbol{x} \in \Gamma(t), \tag{2.3}$$

where T_I is the temperature at the interface,

$$T_I = T_s = T_l, \quad \boldsymbol{x} \in \Gamma(t); \tag{2.4}$$

K is a constant; f is a dimensionless function, which we refer to as the anisotropy function; and ψ is the angle between normal vector at the free surface and the c-axis, as measured relative to the positive x-axis, see Figure 3. Contributions to (2.3) from the surface energy are not included, which we justify by assuming that after the rapid nucleation phase, the radius of the melt is much larger than the capillary length given by $l_{\text{cap}} = (\gamma/\rho L)(T_0/\Delta T)$, where γ is the surface energy of an ice–water interface and ΔT is the local amount of superheating. Takeya [29] measured superheatings on the order of 0.1 K in his experiments that use photographic bulbs as the light source, giving a capillary length of 270 nm; thus, neglecting surface energy seems reasonable given that Tyndall figures typically have length scales on the order of hundreds of microns up to millimetres. An important consequence of neglecting surface energy is that our model will not capture the evolution of the melt into a Wulff shape, which is the equilibrium shape arising from the minimisation of surface energy under constant-volume conditions [10]. However, based on the phase-field simulations by Uehara & Sekera [32], we might expect the melt to grow into its "kinetic Wulff shape", which, in essence, describes the asymptotic shape that the interface would approach if it were to evolve solely due to anisotropic undercooling under isothermal conditions, so that the normal velocity depends only upon the orientation of the interface [32, 35, 36] (also see, below, Sections 3.1 and 3.2).

2.2 The anisotropy function

The anisotropy function f is used to model the orientation dependence of the interfacial velocity arising from the crystalline structure of the ice. We assume that the value of f is close to 1 when the velocity is parallel to the prism planes of the ice crystal and small when the velocity is parallel to the basal planes. Mathematically, this corresponds to $f \sim 1$ when $\psi = \pm\pi/2$, and $f \sim \epsilon \ll 1$ when $\psi = 0, \pm\pi$, respectively. In physical terms, the parameter ϵ can be thought of as the ratio of the melting velocity of basal planes to prism planes for a fixed superheating $T_I - T_0 > 0$. Experimentally, determining a functional form for f is possible by measuring the kinetic Wulff shape. However, acquiring the kinetic Wulff shape is difficult in practice and, consequently, there is often uncertainty in the form of f. Therefore, our analysis will rely on phenomenological expressions for the anisotropy
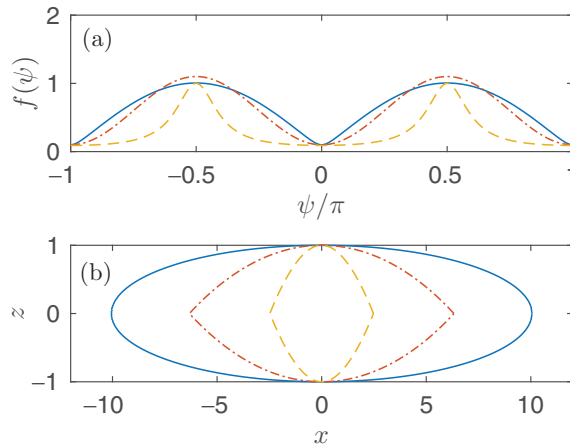
FIGURE 4. Top (a): we consider three different anisotropy functions f that characterise the dependence of the melting rate on the orientation of the solid–liquid interface: $f(\psi) = (\epsilon^2 + \sin^2 \psi)^{1/2}$ (solid), $f(\psi) = \epsilon + \sin^2 \psi$ (dash–dotted), and $f(\psi) = \epsilon/(1 + \epsilon - \sin^2 \psi)$ (dashed). Here, ψ measures the angle between the c-axis and the vector normal to the interface; see Figure 3. Bottom (b): the corresponding kinetic Wulff shapes associated with the three anisotropy functions f, which represent the long-term shape the melt would acquire under isothermal conditions and growth due purely to anisotropic kinetic undercooling. See text for further details. In both panels we have set $\epsilon = 0.1$.

function. More specifically, we will consider in detail the function

$$f(\psi) = (\epsilon^2 + \sin^2 \psi)^{1/2}, \tag{2.5}$$

which is expected to produce smooth interfaces based on its corresponding kinetic Wulff shape. In two dimensions, the kinetic Wulff shape is determined by the convex region containing the origin traced out by the parametric curves

$$x = f'(\psi)\cos\psi + f(\psi)\sin\psi, \tag{2.6a}$$
$$z = f'(\psi)\sin\psi - f(\psi)\cos\psi. \tag{2.6b}$$

The anisotropy function (2.5) is shown along with its corresponding Wulff shape in Figure 4. Additionally, we will present the key results that are obtained when

$$f(\psi) = \epsilon + \sin^2 \psi, \tag{2.7}$$

and

$$f(\psi) = \frac{\epsilon}{1 + \epsilon - \sin^2 \psi}. \tag{2.8}$$

Since $\sin^2 \psi$ can be written in terms of $\sin 2\psi$, the anisotropy function (2.7) is similar to many of those found in the literature [32]. The anisotropy function in (2.8) has sharp maxima at $\psi = \pm\pi/2$ (see Figure 4(a)), making it comparable to theoretical expressions for f that have been derived from models of surface diffusion [5, 35]. Figure 4 shows that the anisotropy functions (2.7) and (2.8) lead to the formation of corners in the kinetic

Table 1. *Parameter values for ice–water systems heated by light from an overhead projector. These are based on experiments carried out in Oxford. The absorption coefficients are for monochromatic infrared radiation with a wavelength of 980 nm. The intensity of radiation is estimated from the power of the bulb and distance to the sample, further details are given in the text*

ρ	1,000 kg/m^3
c_{ps}	2,050 J/(kg K)
c_{pl}	4,181 J/(kg K)
k_s	2 W/(m K)
k_l	0.6 W/(m K)
L	3.33×10^5 J/kg
μ_s	15.3 1/m
μ_l	43.6 1/m
I_0	300 W/m^2
γ	0.033 J/m^2
T_0	273 K

Wulff shape. Surface energy is likely to become important on these small scales and may lead to a smoothing of the corners. Capturing such dynamics is beyond the scope of our current model, however.

2.3 Parameter values

The configuration that we study here is based on experiments involving ice–water systems carried out in Oxford. Light from an overhead projector was used to irradiate a pure ice crystal. A list of parameter values corresponding to these experiments is given in Table 1. Although light from the overhead projector will have a broad spectrum, ice and water are particularly strong absorbers of infrared radiation. Therefore, the absorption coefficients in Table 1 are based on monochromatic infrared radiation with a wavelength of 980 nm. The intensity of radiation has been calculated from the bulb power and distance to the sample by assuming spherical emission; the complete details can be found in Hennessy [15].

Determining values for the parameters K and ϵ is a challenging experimental task. Using arguments from statistical mechanics, it is possible to write the velocities of the planes [34], as well the coefficient K in (2.3) [11], in terms of elementary quantities such as molecular distance and activation energy. However, these expressions introduce additional unknown parameters into the model, making them of little practical use. The combined uncertainty in the values for K and ϵ, as well as in the functional form of the anisotropy function f, will make carrying out a quantitative comparison of our results with experimental data difficult. That being said, qualitative comparisons are still possible, and the analysis can be used as a tool for ruling out anisotropy functions.

2.4 Non-dimensionalisation

The model is non-dimensionalised by introducing suitable scales for time, distance, and temperature. The time variable t is written in terms of the time scale of thermal diffusion

in ice, ℓ^2/κ_s, where $\kappa_s = k_s/(\rho c_{ps})$ is the thermal diffusivity of ice and ℓ is a characteristic length scale defined below. The temperature scale is set by the amount of superheating in the ice caused by volumetric heating, giving $\Delta T = q_s \ell^2/k_s$. Finally, the length scale ℓ is chosen to balance terms in the kinetic condition (2.3), implying that significant growth parallel to the basal planes occurs on $O(1)$ (dimensionless) time scales. This gives $\ell^3 = K k_s^2/(q_s \rho c_{ps})$. Using these scales, we write $t = (\ell^2/\kappa_s)\tau$, $x = \ell X$, and $T_j = T_0 + (\Delta T)\theta_j$. The non-dimensional field equations can be written as

$$\frac{\partial \theta_s}{\partial \tau} = \nabla^2 \theta_s + 1, \quad X \in \Omega_s(\tau), \tag{2.9a}$$

$$\hat{c}_p \frac{\partial \theta_l}{\partial \tau} = \hat{k}\nabla^2 \theta_l + \hat{q}, \quad X \in \Omega_l(\tau), \tag{2.9b}$$

where $\hat{c}_p = c_{pl}/c_{ps}$ and $\hat{k} = k_l/k_s$ are ratios of specific heat capacities and thermal conductivities, respectively. The ratio of volumetric heating, $\hat{q} = q_l/q_s$, can be written in terms of the absorption coefficients via $\hat{q} = \mu_l/\mu_s$. Initial conditions for the temperatures are given by $\theta_s = \theta_l = 0$ at $\tau = 0$.

At the ice–water interface, the Stefan and kinetic conditions, along with the continuity of temperature, are given by

$$v = \beta^{-1}\left(\frac{\partial \theta_s}{\partial n} - \hat{k}\frac{\partial \theta_l}{\partial n}\right), \quad X \in \Gamma(\tau), \tag{2.9c}$$

$$v = \theta_I f(\psi), \quad X \in \Gamma(\tau), \tag{2.9d}$$

$$\theta_I = \theta_s = \theta_l, , \quad X \in \Gamma(\tau), \tag{2.9e}$$

respectively, where $\beta = L/(c_{ps}\Delta T)$ is the Stefan number. The initial ice–water interface is taken to be the sphere with dimensionless radius $\alpha = a/\ell$ given by $|X| = \alpha$.

Far from a growing liquid inclusion, $\partial \theta_s/\partial \tau \sim 1$, so that we have

$$\theta_s \sim \tau, \quad |X| \to \infty. \tag{2.9f}$$

Note that (2.9f) requires that the Tyndall figure and associated length scales be small compared with the region subject to the body heating.

Using the parameter values in Table 1, we find that $\hat{k} \simeq 0.3$, $\hat{c}_p \simeq 2$, and $\hat{q} \simeq 3$, all of which can be treated as $O(1)$ in size. Due to uncertainty in the value of the parameter K, it is difficult to estimate the length scale ℓ, the characteristic temperature rise ΔT, and the Stefan number β. Using instead the measured value of $\Delta T \sim 0.1$ K from Takeya [29], the Stefan number is given by $\beta \sim 10^3$. The length scale can be estimated from $\ell = (\Delta T k_s/q_s)^{1/2} \sim 6.7$ mm and the time scale from $\ell^2/\kappa_s \sim 46$ s, which seem slightly large but reasonable.

The proceeding analysis will focus on the distinguished limit whereby $\epsilon = O(\beta^{-1})$. This regime is considered so that we can examine the interplay of the kinetic anisotropic effects; whether or not this balance occurs in practice depends upon the size of the rate of the volumetric heating. Thus, we write $\beta^{-1} = b\epsilon$, where $b = O(1)$. Furthermore, it will be assumed that the (dimensionless) radius of the initial melt, α, satisfies $\alpha \ll \epsilon$. In dimensional terms, this inequality means that the initial radius should be less than

1 μm, which is close to the limit where surface-energy effects become important. This upper bound on the initial size of the radius, along with the anisotropic kinetic condition (2.9e), ensures that the spherical Tyndall figure will first grow into a thin disc of melt with radius that is much greater than its thickness, which is consistent with experimental observations [29].

3 Analysis

The analysis begins in Section 3.1 with an examination of the small-time behaviour for $\tau = O(\alpha^{1/2})$. In dimensional terms, the small-time regime corresponds to times given by $t \sim (a/\ell)^{1/2}(\ell^2/\kappa_s)$. Taking the dimensional radius of the initial melt to be of the order of one micron, we find that $t \sim 0.5$ seconds. In this regime, the volumetric heating and the kinetic condition drive the melt into a thin shape with dimensions along the c-axis that are much smaller than those in the basal plane. In Section 3.2, we consider the dynamics when $\tau = O(1)$, corresponding to $t \sim 50$ seconds. By exploiting the separation of length scales that arises from the initial growth, a simplified model can be derived. Using this model, the linear stability of the ice–water interface is examined in Section 3.3. Our analysis will first focus on the dynamics that occur when the anisotropy function (2.5) is used. We will then consider additional anisotropy functions in Section 3.4.

3.1 Early time

The analysis of the early-time behaviour proceeds by letting $\tau = \alpha^{1/2}\bar{\tau}$, $\theta_j = \alpha^{1/2}\bar{\theta}_j$, where $\alpha \ll \epsilon \ll 1$. We then consider the temperature field near and away from the melt, and connect the solutions in the two regions using asymptotic matching.

In the region of solid away from the melt, i.e., for $X \sim O(1)$, the leading-order problem in α is straightforward to solve and it gives $\bar{\theta}_s(X, \bar{t}) = \bar{\tau}$. To resolve the temperatures near the melt, we let $X = \alpha\bar{X}$. The leading-order problem in α in this inner region is given by

$$\nabla^2 \bar{\theta}_s = 0, \quad \bar{X} \in \bar{\Omega}_s(\bar{\tau}), \tag{3.1}$$

$$\nabla^2 \bar{\theta}_l = 0, \quad \bar{X} \in \bar{\Omega}_l(\bar{\tau}) \tag{3.2}$$

with the following conditions at the solid–liquid interface:

$$\frac{\partial \bar{\theta}_l}{\partial n} = \hat{k}\frac{\partial \bar{\theta}_s}{\partial n}, \quad \bar{X} \in \bar{\Gamma}(\bar{\tau}), \tag{3.3}$$

$$\bar{v} = \bar{\theta}_I f(\psi), \quad \bar{X} \in \bar{\Gamma}(\bar{\tau}). \tag{3.4}$$

By asymptotically matching the temperatures in the solid, we also have that $\bar{\theta}_s \to \bar{\tau}$ as $|\bar{X}| \to \infty$. The solutions for the temperature fields are given by $\bar{\theta}_l = \bar{\theta}_s \equiv \bar{\tau}$. The motion of the interface, therefore, satisfies the equation

$$\bar{v} = \bar{\tau}f(\psi). \tag{3.5}$$

To make further progress, we suppose that the rescaled positions of the ice–water

interface are given by the zero level set of a function F, defined by

$$F = \bar{s}(\bar{X}(\bar{\tau})) - \bar{\tau}^2/2 \equiv 0, \tag{3.6}$$

where $\bar{s}$ a function that is to be determined. The initial shape of the interface is encoded in the function $\bar{s}$; we require that $\bar{s}(\bar{X}(0)) \equiv 0$ on the sphere $|\bar{X}| = 1$ when $\bar{\tau} = 0$. We emphasise here that $\bar{s}$ also plays the role of a time variable; from (3.6) we see that $\bar{s} = \bar{\tau}^2/2$. In this formulation, the normal velocity at the interface can be written as $\bar{v} = \bar{\tau}/|\nabla \bar{s}|$ and, therefore, the kinetic condition (3.5) becomes

$$|\nabla \bar{s}| f(\psi) = 1. \tag{3.7}$$

Closing the problem requires writing the angle ψ in terms of the function $\bar{s}$. For clarity, we now consider the two-dimensional problem by writing $\bar{X} = (\bar{X}, 0, \bar{Z})$. In this case, simple trigonometry shows that the angle ψ satisfies $\sin \psi = \bar{s}_{\bar{X}}/(\bar{s}_{\bar{X}}^2 + \bar{s}_{\bar{Z}}^2)^{1/2}$, where $\bar{s}_{\bar{X}} = \partial \bar{s}/\partial \bar{X}$ and $\bar{s}_{\bar{Z}} = \partial \bar{s}/\partial \bar{Z}$. By writing $f(\psi) = \hat{f}(\sin \psi)$, the kinetic equation (3.7) becomes

$$(\bar{s}_{\bar{X}}^2 + \bar{s}_{\bar{Z}}^2)^{1/2} \hat{f}\left(\bar{s}_{\bar{X}}(\bar{s}_{\bar{X}}^2 + \bar{s}_{\bar{Z}}^2)^{-1/2}\right) = 1. \tag{3.8}$$

To see how the melt region evolves, we now focus on the anisotropy function given by (2.5). In this case, the problem for $\bar{s}$ is

$$(\bar{s}_{\bar{X}}^2 + \bar{s}_{\bar{Z}}^2)^{1/2} \left[\epsilon^2 + \bar{s}_{\bar{X}}^2(\bar{s}_{\bar{X}}^2 + \bar{s}_{\bar{Z}}^2)^{-1}\right]^{1/2} = 1 \tag{3.9}$$

subject to the condition $\bar{s}(\bar{X}_0, \bar{Z}_0) \equiv 0$ on the circle $\bar{X}_0^2 + \bar{Z}_0^2 = 1$ at time $\bar{\tau} = 0$. The solution to this problem can be found using Charpit's equations, as detailed in Appendix A. In essence, Charpit's equations are a generalisation of the method of characteristics for non-linear first-order hyperbolic problems. We proceed by parametrising the initial data according to $\bar{X}_0(\varphi) = (\bar{X}_0, \bar{Z}_0) = (\cos \varphi, \sin \varphi)$, $\bar{s}(\bar{X}_0(\varphi)) \equiv 0$, with $\varphi \in [0, 2\pi]$. Upon applying the method, solution can be written implicitly and parametrically as

$$\bar{X} = \left[1 + \frac{\bar{s}(1 + \epsilon^2)}{(\epsilon^2 + \cos^2 \varphi)^{1/2}}\right] \cos \varphi, \quad \bar{Z} = \left[1 + \frac{\bar{s}\epsilon^2}{(\epsilon^2 + \cos^2 \varphi)^{1/2}}\right] \sin \varphi. \tag{3.10}$$

Thus, for a given value of $\bar{s}$, which can be written in terms of time via $\bar{s} = \bar{\tau}^2/2$, these curves trace out the instantaneous positions of the solid–liquid interface as φ is varied from 0 to 2π. Figure 5 shows the interface profiles predicted by (3.10) at various times when $\epsilon = 0.1$. The initially spherical melt first grows primarily in the radial direction, keeping its thickness in the axial direction constant (top panel). By the time the axial growth becomes appreciable, the radius of the melt has grown a substantial amount, resulting in a liquid region with a small aspect ratio.

To aid in the physical interpretation of (3.10), we revert to the original non-dimensionalisation by writing $\bar{s} = s/\alpha$, $\bar{X} = X/\alpha$, $\bar{\tau} = \tau/\alpha^{1/2}$ to obtain

$$X = \left[\alpha + \frac{s(1 + \epsilon^2)}{(\epsilon^2 + \cos^2 \varphi)^{1/2}}\right] \cos \varphi, \quad Z = \left[\alpha + \frac{s\epsilon^2}{(\epsilon^2 + \cos^2 \varphi)^{1/2}}\right] \sin \varphi, \tag{3.11}$$
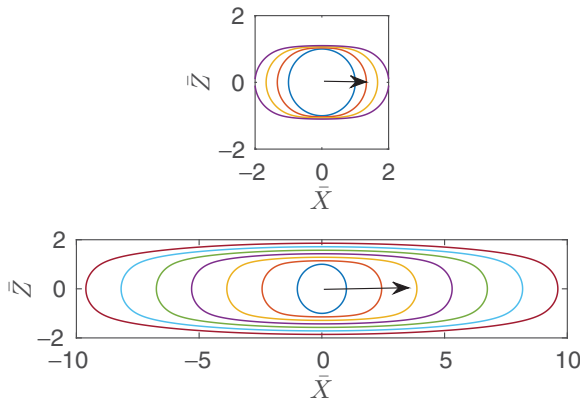
FIGURE 5. The early-time evolution of a spherical melt figure when the anisotropy function is given by (2.5) when $\epsilon = 0.1$. These curves are given by the solution in (3.10). The arrows indicates the direction of time. The top panels shows the solid–liquid interface at equally spaced values of $\bar{s}$ given by $\bar{s} = 0, 0.33, 0.66,$ and 1, corresponding to rescaled dimensionless times given by $\bar{\tau} = (2\bar{s})^{1/2} = 0,$ 0.82, 1.15, and 1.41, respectively. Similarly, the bottom panel shows the interface for values of $\bar{s}$ given by $\bar{s} = 0, 1.42, 2.86, 4.29, 5.71, 7.14,$ and 8.57, corresponding to $\bar{\tau} = 0, 1.69, 2.39, 2.93, 3.38,$ 3.78, and 4.14. The interface remains smooth for all time and evolves into the kinetic Wulff shape shown in Figure 4.

where $s = \tau^2/2$. In the very early stages of development, so that s is of order α, then for parts of the interface given by $|\cos\varphi| \gg \epsilon$,

$$Z \sim \alpha\sin\varphi, \quad X \sim \left(\alpha + \frac{s}{|\cos\varphi|}\right)\cos\varphi \sim \pm s + \alpha\cos\varphi, \tag{3.12}$$

while for $|\cos\varphi| = O(\epsilon)$, say $\varphi = \pm\pi/2 \mp \psi$ with $\psi = O(\epsilon)$,

$$Z \sim \pm\alpha, \quad X \sim \pm\left(\alpha \pm \frac{s}{\epsilon^2 + \psi^2}\right)\psi \sim \frac{\pm\psi s}{(\epsilon^2 + \psi^2)^{1/2}}. \tag{3.13}$$

Thus, the interface takes the form, approximately, of two circular arcs, each of radius α and centred on $(X, Z) = (\pm s, 0)$, linked by horizontal lines.

In the later stages, $s \gg \alpha/\epsilon$,

$$Z \sim \frac{\epsilon^2 s}{(\epsilon^2 + \cos^2\varphi)^{1/2}}\sin\varphi, \quad X \sim \frac{s(1 + \epsilon^2)}{(\epsilon^2 + \cos^2\varphi)^{1/2}}\cos\varphi, \tag{3.14}$$

and

$$\frac{X^2}{1 + \epsilon^2} + \frac{Z^2}{\epsilon^2} \sim \frac{s^2}{\epsilon^2 + \cos^2\varphi}[(1 + \epsilon^2)\cos^2\varphi + \epsilon^2\sin^2\varphi] = s^2, \tag{3.15}$$

so the interface is then approximately elliptical. The longer-term interface profile, defined by the large-time limit of the small-time model, and given by (3.14) for this choice of f, is, in fact, equivalent to the corresponding kinetic Wulff shape that can be computed from (2.6). Note that the half thickness of the melt, given by the maximum value of Z, grows
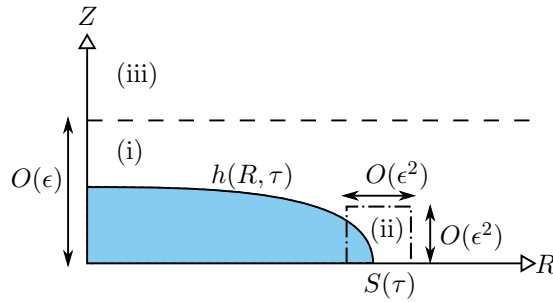
FIGURE 6. A schematic diagram showing the three asymptotic regions in the $\tau = O(1)$ problem. By constructing local solutions in regions (i) and (ii), it is possible to derive effective boundary conditions that lead to a self-contained problem in region (iii) by asymptotic matching.

in time as $Z(\varphi = \pi/2) = \epsilon\tau^2/2$. The maximum value of X, corresponding to the rim of the melt, grows as $X(\varphi = 0) \sim \tau^2/2$. We see that for $s \gg \alpha$, the influence of the initial interface has been lost.

3.2 Order-one time

We now consider the dynamics that occur on $O(1)$ time scales. The initial condition in this time regime takes the form of a matching requirement, as $\tau \to 0$, with the fully developed early-time shape given by (3.15). The analysis in two and three dimensions is sufficiently similar for us to proceed directly to problems with axial symmetry. Thus, we define a radial coordinate $R = (X^2 + Y^2)^{1/2}$. We also assume the system remains symmetric about the $Z = 0$ plane and, thus, we only consider the problem in the upper-half space given by $Z > 0$. The position of the solid–liquid interface is written as $Z = h(R, \tau)$; the corresponding position of the rim is $R = S(\tau)$ so that $h(S(\tau), \tau) \equiv 0$. The angle ψ appearing in the anisotropy function f satisfies

$$\sin\psi = \frac{\partial h/\partial R}{(1 + (\partial h/\partial R)^2)^{1/2}}. \tag{3.16}$$

From matching into the early-time regime and using (3.15), we expect that

$$h(R) \sim \epsilon(S^2 - R^2)^{1/2} \tag{3.17}$$

as $\tau \sim 0$.

In principle, the dynamics in the $O(1)$ time regime can be studied by solving (2.9) directly. However, the thin aspect ratio of the melt, with $Z \sim O(\epsilon)$ and $X, Y \sim O(1)$, motivates seeking a solution via matched asymptotic expansions, and this is the approach we take. There are three distinct regions that need to be considered: (i) near the melt but away from the rim, (ii) near the melt and near the rim, and (iii) away from the melt. A schematic diagram of these regions is shown in Figure 6. Our approach is to obtain local solutions in regions (i) and (ii) which can then be used to derive effective boundary conditions for the problem in region (iii) by asymptotic matching.

3.2.1 *Analysis near the melt and away from the rim*

In region (i) near the melt but away from the rim, $R \ll S(\tau)$, we rescale the axial coordinate according to $Z = \epsilon \tilde{Z}$. In addition, the position of the interface is written as $h(R, \tau) = \epsilon \tilde{h}(R, \tau)$ and the temperatures in this region are denoted by $\tilde{\Theta}_j$, $j = l, s$. Under this scaling, the anisotropy function (2.5) can be written as $f(\psi) \sim \epsilon[1 + (\partial \tilde{h}/\partial R)^2]^{1/2}$. The governing equations in this region are given by

$$\epsilon^2 \frac{\partial \tilde{\Theta}_s}{\partial \tau} = \frac{\epsilon^2}{R} \frac{\partial}{\partial R} \left(R \frac{\partial \tilde{\Theta}_s}{\partial R} \right) + \frac{\partial^2 \tilde{\Theta}_s}{\partial \tilde{Z}^2} + \epsilon^2, \quad \tilde{Z} > \tilde{h}(R, \tau), \tag{3.18a}$$

$$\epsilon^2 \hat{c}_p \frac{\partial \tilde{\Theta}_l}{\partial \tau} = \frac{\epsilon^2 \hat{k}}{R} \frac{\partial}{\partial R} \left(R \frac{\partial \tilde{\Theta}_l}{\partial R} \right) + \hat{k} \frac{\partial^2 \tilde{\Theta}_l}{\partial \tilde{Z}^2} + \epsilon^2 \hat{q}, \quad \tilde{Z} < \tilde{h}(R, \tau). \tag{3.18b}$$

The boundary conditions on the solid–liquid interface are

$$\epsilon b^{-1} \frac{\partial h}{\partial \tau} = -\hat{k} \left(\frac{\partial \tilde{\Theta}_l}{\partial \tilde{Z}} - \epsilon^2 \frac{\partial \tilde{\Theta}_l}{\partial R} \frac{\partial \tilde{h}}{\partial R} \right) + \frac{\partial \tilde{\Theta}_s}{\partial \tilde{Z}} - \epsilon^2 \frac{\partial \tilde{\Theta}_s}{\partial R} \frac{\partial \tilde{h}}{\partial R}, \quad \tilde{Z} = \tilde{h}(R, \tau), \tag{3.18c}$$

$$\frac{\partial \tilde{h}}{\partial \tau} = \tilde{\Theta}_I \left[1 + \left(\frac{\partial \tilde{h}}{\partial R} \right)^2 \right]^{1/2} \left[1 + \epsilon^2 \left(\frac{\partial \tilde{h}}{\partial R} \right)^2 \right]^{1/2}, \quad \tilde{Z} = \tilde{h}(R, \tau), \tag{3.18d}$$

where $\tilde{\Theta}_I = \tilde{\Theta}_s(R, \tilde{h}(R, \tau), \tau) = \tilde{\Theta}_l(R, \tilde{h}(R, \tau), \tau)$. The symmetry about $\tilde{Z} = 0$ implies that $\partial \tilde{\Theta}_l / \partial \tilde{Z} = 0$ at $\tilde{Z} = 0$. The relevant matching conditions for the temperature in the solid as $\tilde{Z} \to \infty$ will be discussed below.

The solution to this problem is now expanded as

$$\tilde{\Theta}_j = \tilde{\Theta}_j^{(0)} + \epsilon \tilde{\Theta}_j^{(1)} + O(\epsilon^2), \tag{3.19a}$$

$$\tilde{h} = \tilde{h}^{(0)} + \epsilon \tilde{h}^{(1)} + O(\epsilon^2). \tag{3.19b}$$

Assuming that $\epsilon^2 \hat{q} = O(\epsilon^2)$, the $O(1)$ solution for the temperature is straightforward to obtain and is given by

$$\tilde{\Theta}_l^{(0)}(R, \tilde{Z}, \tau) = \tilde{\Theta}_s^{(0)}(R, \tilde{Z}, \tau) \equiv \tilde{\Theta}_I^{(0)}(R, \tau). \tag{3.20}$$

The matching condition for this problem is given by $\tilde{\Theta}_s^{(0)}(R, \tilde{Z}, \tau) = \theta_s(R, 0, \tau)$ as $\tilde{Z} \to \infty$. From (3.20), we can deduce that $\tilde{\Theta}_I^{(0)}(R, \tau) = \theta_s(R, 0, \tau)$. Therefore, the $O(1)$ part of the kinetic equation (3.18d) becomes

$$\frac{\partial \tilde{h}^{(0)}}{\partial \tau} = \theta_s(R, 0, \tau) \left[1 + \left(\frac{\partial \tilde{h}^{(0)}}{\partial R} \right)^2 \right]^{1/2}. \tag{3.21}$$

Proceeding to the $O(\epsilon)$ problem, we find that the temperatures are determined from bulk equations

$$\frac{\partial^2 \tilde{\Theta}_j^{(1)}}{\partial \tilde{Z}^2} = 0 \tag{3.22}$$

and must satisfy the Stefan condition

$$b^{-1}\frac{\partial \tilde{h}^{(0)}}{\partial \tau} = -\hat{k}\frac{\partial \tilde{\Theta}_l^{(1)}}{\partial \tilde{Z}} + \frac{\partial \tilde{\Theta}_s^{(1)}}{\partial \tilde{Z}}. \tag{3.23}$$

By exploiting the symmetry of the problem about the Z-axis, we find that the temperature in the liquid, $\tilde{\Theta}_l^{(1)}$, must be constant in space. Asymptotically matching the derivatives of the solid temperature in regions (i) and (iii) gives the relation

$$\frac{\partial \theta_s^{(1)}}{\partial \tilde{Z}} = \frac{\partial \theta_s}{\partial z} \tag{3.24}$$

as $\tilde{Z} \to \infty$ and $z \to 0$. Using (3.24) in the Stefan condition, (3.23) yields

$$\frac{\partial \tilde{h}^{(0)}}{\partial \tau} = b\frac{\partial \theta_s}{\partial z}, \quad z = 0. \tag{3.25}$$

We emphasise here that (3.21) and (3.25) can be treated as boundary conditions for the problem in region (iii) away from the melt.

3.2.2 Analysis near the melt and near the rim

The next step is to consider the local dynamics near the rim in order to derive an equation describing its motion. We switch to a travelling-wave coordinate given by $\check{R} = (R-S(\tau))/\epsilon^2$ and let $Z = \epsilon^2\check{Z}$. These scales have been chosen in order to balance both sides of the initial interface profile given in (3.17). The position of the solid–liquid interface is written as $h(R, \tau) = \epsilon^2\check{h}(\check{R})$ and the temperatures are denoted by $\check{\Theta}_j$ for $j = l, s$. Upon using this scaling in (2.9), the leading-order problem in ϵ is given by

$$\frac{\partial^2 \check{\Theta}_j}{\partial \check{R}^2} + \frac{\partial^2 \check{\Theta}_j}{\partial \check{Z}^2} = 0, \quad (\check{R}, \check{Z}) \in \check{\Omega}_j(\tau), \quad j = s, l. \tag{3.26}$$

The Stefan condition reduces to the continuity of thermal flux across the interface

$$\frac{\partial \check{\Theta}_s}{\partial \check{Z}} - \frac{\partial \check{\Theta}_s}{\partial \check{R}}\frac{\partial \check{h}}{\partial \check{R}} = \hat{k}\left(\frac{\partial \check{\Theta}_l}{\partial \check{Z}} - \frac{\partial \check{\Theta}_l}{\partial \check{R}}\frac{\partial \check{h}}{\partial \check{R}}\right), \quad \check{Z} = \check{h}(\check{R}), \quad \check{R} < 0. \tag{3.27}$$

The leading-order kinetic equation reads

$$-\frac{\mathrm{d}S}{\mathrm{d}\tau}\frac{\mathrm{d}\check{h}}{\mathrm{d}\check{R}} = \check{\Theta}_I\left|\frac{\partial \check{h}}{\partial \check{R}}\right|, \quad \check{Z} = \check{h}(\check{R}), \quad \check{R} < 0, \tag{3.28}$$

where $\check{\Theta}_I = \check{\Theta}_s(\check{R}, \check{h}(\tau), \tau) = \check{\Theta}_l(\check{R}, \check{h}(\tau), \tau)$. Since the thickness of the melt needs to decrease to zero as the rim is approached, we expect that $\partial \check{h}/\partial \check{R} < 0$ for all $\check{R} < 0$; therefore, the kinetic condition (3.28) reduces to

$$\frac{\partial S}{\partial \tau} = \check{\Theta}_I(\check{R}, \tau), \quad \check{R} < 0. \tag{3.29}$$

Furthermore, we have the symmetry conditions

$$\frac{\partial \check{\Theta}_l}{\partial \check{Z}} = 0, \quad \check{Z} = 0, \quad \check{R} < 0, \tag{3.30a}$$

$$\frac{\partial \check{\Theta}_s}{\partial \check{Z}} = 0, \quad \check{Z} = 0, \quad \check{R} > 0. \tag{3.30b}$$

By matching to the solutions in region (ii), we obtain the following far-field conditions:

$$\check{\Theta}_l = \check{\Theta}_s \sim \theta_s(S(\tau), 0, \tau). \tag{3.31}$$

It is straightforward to see that the bulk equations (3.26) and the Stefan condition (3.27) are satisfied by temperatures that are constant in space. Therefore, we have that

$$\check{\Theta}_l = \check{\Theta}_s \equiv \theta_s(S(\tau), 0, \tau) \tag{3.32}$$

to leading order, which implies the rim moves according to

$$\frac{\partial S}{\partial \tau} = \theta_s(S(\tau), 0, \tau). \tag{3.33}$$

The next-order problem can be used to determine the profile of the melt near the rim; however, this is not required in the subsequent analysis. Finally, we note that by matching the melt heights in regions (ii) and (iii), i.e., $\epsilon \tilde{h}$ and $\epsilon^2 \check{h}$, we find that

$$\tilde{h}^{(0)} \sim 0, \quad R \sim S(\tau). \tag{3.34}$$

We now have all of the ingredients to write down a self-contained problem in region (iii).

3.2.3 *A reduced model for $O(1)$ times*

In region (iii), the melt appears to have zero thickness; it has been collapsed onto a circle lying within the $Z = 0$ plane. The asymptotic matching into the inner regions (i) and (ii) provides boundary conditions on this circle. Although the melt is effectively treated as having zero thickness, the model still captures its evolving shape.

In region (iii), the temperature field satisfies the equation

$$\frac{\partial \theta_s}{\partial \tau} = \nabla^2 \theta_s + 1, \quad Z > 0 \tag{3.35a}$$

with $\theta_s = 0$ when $\tau = 0$. In the far-field, we require that $\theta_s \sim \tau$ as $|X| \to \infty$. The $Z = 0$ plane is divided into two regions corresponding to being inside and outside of the melt, $R < S(\tau)$ and $R > S(\tau)$, respectively. For points inside of the melt, we have Stefan and anisotropic kinetic conditions given by (where we drop the (0) subscript on $\tilde{h}^{(0)}$)

$$\frac{\partial \tilde{h}}{\partial \tau} = b \frac{\partial \theta_s}{\partial Z}, \qquad Z = 0, \ R < S(\tau), \tag{3.35b}$$

$$\frac{\partial \tilde{h}}{\partial \tau} = \theta_s \left[1 + \left(\frac{\partial \tilde{h}}{\partial R} \right)^2 \right]^{1/2}, \quad Z = 0, \ R < S(\tau). \tag{3.35c}$$

It should be noted that, because of (3.35*b*), the Stefan condition plays a significant rôle in this regime. This means that the isothermal approximation fails to hold and the melt region should no longer be expected to take a kinetic Wulff shape.

Outside of the melt, we impose a symmetry condition given by

$$\frac{\partial \theta_s}{\partial Z} = 0, \quad Z = 0, \ R > S(\tau). \tag{3.35d}$$

The kinetic condition at the rim reads

$$\frac{\partial S}{\partial \tau} = \theta_s, \quad Z = 0, \ R = S(\tau). \tag{3.35e}$$

Finally, it is required that

$$\tilde{h}(S(\tau), 0, \tau) = 0. \tag{3.35f}$$

To determine asymptotically consistent initial conditions for the position of the rim and the profile of the solid–liquid interface, we examine the early behaviour of (3.35) and match it to the small-time solution given by (3.15).

3.2.4 *Early behaviour of model for* $O(1)$ *times*

The relevant scaling to resolve the early time behaviour and match into the small-time regime is given by $\tau = \epsilon^{1/2}\hat{\tau}$, $\theta_s = \epsilon^{1/2}\hat{\theta}_s$, $X = \epsilon\hat{X}$, $\tilde{h} = \epsilon\hat{h}$, and $S = \epsilon\hat{S}$. From the leading-order problem in ϵ, it is straightforward to deduce that $\hat{\theta} = \hat{\tau}$. The leading-order kinetic conditions that hold within the melt and at the rim are then given by

$$\frac{\partial \hat{h}}{\partial \hat{\tau}} = \hat{\tau} \left[1 + \left(\frac{\partial \hat{h}}{\partial \hat{R}} \right) \right]^{1/2}, \tag{3.36a}$$

$$\frac{\partial \hat{S}}{\partial \hat{\tau}} = \hat{\tau}. \tag{3.36b}$$

From (3.15), we see that in the small-time regime, the rim grows like $\tau^2/2 + O(\epsilon)$ for $\tau \sim O(1)$; therefore, we can solve (3.36*b*) and by matching we obtain $\hat{S}(\hat{\tau}) = \hat{\tau}^2/2$. The solution for $\hat{S}$ motivates seeking a similarity solution to (3.36*a*) of the form $\hat{h} = \hat{\tau}^2\hat{H}(\hat{R}/\hat{\tau}^2)$. Using this ansatz in (3.36*a*) gives the problem

$$2 \left[\hat{H}(\zeta) - \zeta\hat{H}'(\zeta) \right] = \left[1 + (\hat{H}'(\zeta))^2 \right]^{1/2}, \tag{3.37}$$

where $\zeta = \hat{R}/\hat{\tau}^2$ and $\hat{H}$ satisfies $\hat{H}(1/2) = 0$. The solution is $\hat{H}(\zeta) = A(1/4 - \zeta^2)^{1/2}$ or, equivalently

$$\hat{h} = A \left(\frac{\hat{\tau}^4}{4} - \hat{R}^2 \right)^{1/2}, \tag{3.38}$$

where $A = 1$ is a constant that can be determined by matching to (3.15) as $\tau \sim O(1)$. From this analysis, we can conclude that the model in (3.35) should have initial conditions for

the interface given by

$$\tilde{h} \sim \left(\frac{\tau^4}{4} - R^2 \right)^{1/2}, \quad S \sim \frac{\tau^2}{2} \tag{3.39}$$

as $\tau \sim 0$. For $0 < \tau \ll 1$, (3.39) describes the early growth of the melt in the $O(1)$ time regime, which is consistent with the long-term growth in the first time regime.

3.3 Linear stability for times of $O(1)$

We now examine the linear stability of the system using the reduced model (3.35). The calculation involves two main steps. First, a base state corresponding to a growing axisymmetric melt is computed. Finally, we determine the growth rates of small, azimuthally varying perturbations to the base state. Our analysis will focus on constructing local solutions valid near, but not too close to, the rim.

Our calculation of the base state begins by introducing a travelling-wave coordinate $\check{X}$ such that $\check{X} = R - S(\tau)$ and letting $\check{Z} = Z$. We focus on the local behaviour of solutions near the rim so that $\check{X}^2 + \check{Z}^2 \ll 1$. The temperature and the melt thickness are written as $\theta_s \sim \check{\theta}_s(\check{X}, \check{Z})$ and $h \sim \check{h}(\check{X})$, where we expect from (3.17) that $\check{h}(\check{X}) \sim \check{h}_1(-\check{X})^{1/2}$ for sufficiently small $\check{X}$.

Close to the rim, the temperature $\check{\theta}_s$ approximately satisfies Laplace's equation

$$\frac{\partial^2 \check{\theta}_s}{\partial \check{X}^2} + \frac{\partial^2 \check{\theta}_s}{\partial \check{Z}^2} = 0. \tag{3.40}$$

The Stefan and kinetic conditions read

$$-\frac{\partial S}{\partial \tau} \frac{\partial \check{h}}{\partial \check{X}} = b \frac{\partial \check{\theta}_s}{\partial \check{Z}}, \qquad \check{Z} = 0, \ \check{X} < 0, \tag{3.41}$$

$$-\frac{\partial S}{\partial \tau} \frac{\partial \check{h}}{\partial \check{X}} = \check{\theta}_s \left[1 + \left(\frac{\partial \check{h}}{\partial \check{X}} \right)^2 \right]^{1/2}, \quad \check{Z} = 0, \ \check{X} < 0, \tag{3.42}$$

respectively. The symmetry condition is given by

$$\frac{\partial \check{\theta}_s}{\partial \check{Z}} = 0, \quad \check{Z} = 0, \ \check{X} > 0 \tag{3.43}$$

and the rim evolves according to

$$\frac{\partial S}{\partial \tau} = \check{\theta}_s, \quad \check{Z} = 0, \ \check{X} = 0. \tag{3.44}$$

Since we have assumed that $\check{\theta}_s$ is independent of τ, we immediately deduce from (3.44) that the rim moves with a constant velocity, V, given by $V = \check{\theta}_s(0,0)$.
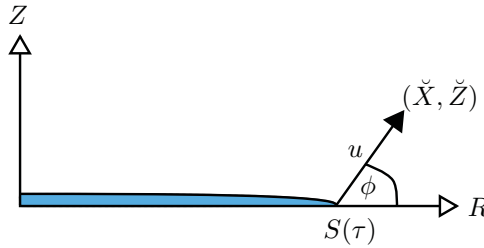
FIGURE 7. A schematic diagram of the local polar coordinates given by $\check{X} = u\cos\phi$ and $\check{Z} = u\sin\phi$ that are centred at the rim. It is convenient to write the local temperature profile in terms of these coordinates; see text for details.

An approximate solution for the temperature can be obtained by converting to local polar coordinates that are centred at the rim. Thus, we introduce the change of variable

$$\check{X} = u\cos\phi, \quad \check{Z} = u\sin\phi, \tag{3.45}$$

where u is the local radius and ϕ is the polar angle measured relative to the positive $\check{X}$-axis; see Figure 7.

An approximate solution for the temperature can be written as

$$\check{\theta}_s \sim V + \check{\theta}_1 u^{1/2}\cos(\phi/2) + \gamma\check{X}, \tag{3.46}$$

which satisfies the symmetry condition (3.43) and where $\check{\theta}_1$ is a constant that can be determined from the Stefan condition (3.41). In particular, by inserting (3.46) in (3.41) and using the fact that $\check{h} \sim \check{h}_1(-\check{X})^{1/2}$ for $\check{X} \sim 0^-$, we find

$$\frac{1}{2}V\check{h}_1(-\check{X})^{-1/2} \sim \frac{1}{2}\check{\theta}_1(-\check{X})^{-1/2}, \quad \check{X} \sim 0^- \tag{3.47}$$

so that $\check{\theta}_1 = V\check{h}_1$. Using a similar procedure in the kinetic condition (3.42) shows that $\check{h}_1 = 1$. The parameter γ in (3.46) is taken to be a free parameter and we will investigate the role it plays in controlling the stability of the problem.

We now investigate the stability of the base state by adding small perturbations of order $\delta \ll 1$ to $\check{\theta}_s$ and S. To simplify matters, we suppose that we are looking locally near $(X, Y, Z) = (V\tau + \check{X}, \check{Y}, \check{Z})$, where $\check{X}^2 + \check{Y}^2 + \check{Z}^2 \ll 1$, and can consider the rim as a straight line on these scales. Taking the rim to be flat is reasonable when the perturbation wavenumber in the azimuthal direction is large. Note that $\check{X} = \check{Y} = \check{Z} = 0$ corresponds to a point on the base-state rim and, thus, we have effectively attached a Cartesian coordinate system to this point. We write the local temperature and the position of the rim as

$$\theta_s \sim \check{\theta}_s(\check{X}, \check{Z}) + \delta\check{\Theta}_s(\check{X}, \check{Z})\,e^{i\kappa\check{Y}+m\tau}, \tag{3.48a}$$

$$S \sim V\tau + \delta\check{S}\,e^{i\kappa\check{Y}+m\tau}, \tag{3.48b}$$

where κ and m denote the wavenumber and growth rate of the perturbations, respectively,

and $\check{\theta}_s$ is given by (3.46). The perturbation to the temperature satisfies the equation

$$\frac{\partial^2 \check{\Theta}_s}{\partial \check{X}^2} + \frac{\partial^2 \check{\Theta}_s}{\partial \check{Z}^2} - \kappa^2 \check{\Theta}_s = 0 \tag{3.49}$$

together with

$$\frac{\partial \check{\Theta}_s}{\partial \check{Z}} = 0, \quad \check{Z} = 0, \ \check{X} > 0. \tag{3.50}$$

The solution can be found using the local polar coordinates in (3.45) and written as

$$\check{\Theta}_s = \check{\Theta}_1 u^{-1/2} e^{-\kappa u} \cos(\phi/2), \tag{3.51}$$

where $\check{\Theta}_1$ is a constant that is to be determined. An equation governing the perturbation to the rim position can be derived from inserting (3.48) into the kinetic condition $\partial S/\partial \tau = \theta_s(S(\tau), \tau)$, expanding about $\delta \ll 1$, and taking the $O(\delta)$ part

$$m\check{S} = \frac{\partial \check{\theta}_s}{\partial \check{X}} \check{S} + \check{\Theta}_s, \quad \check{Z} = 0, \ \check{X} = 0. \tag{3.52}$$

We note that

$$\frac{\partial \check{\theta}_s}{\partial \check{X}} \sim \frac{V}{2} \check{X}^{-1/2} + \gamma, \quad \check{\Theta}_s \sim \check{\Theta}_1 \check{X}^{-1/2} \tag{3.53}$$

as $\check{X} \sim 0$ and $\check{Z} = 0$, both of which become singular as $\check{X} \to 0$. In order for the kinetic condition (3.52) to remain well defined, we need $\check{\Theta}_1 = -(V/2)\check{S}$, which yields

$$m\check{S} = \gamma\check{S}, \tag{3.54}$$

i.e., the perturbation growth rate m is exactly equal to the parameter γ in the base-state temperature profile (3.46). This linear analysis thus indicates instability if there is a background temperature gradient in the direction of propagation of the rim, $\gamma > 0$, but stability for a negative gradient, $\gamma < 0$. Note that in the case of instability, the growth rate of the perturbations is independent of the wave number, in contrast to unstable Hele–Shaw or Stefan problems without surface tension/energy, where growth rate increases with wave number and can be arbitrarily high. Note that similar stability results for another free boundary problem were obtained in Howison *et al.* [16].

Given the absence of exact and of approximate long-time solutions about which to perturb, it is not immediately apparent what values γ might take in practice. Intuitively we might expect γ to be positive, since melting at the interface has the effect of locally reducing temperature, at least for relatively low times τ. The simulations by Hennessy [15] support this claim, although they do not consider heat transfer in the axial direction. If γ is positive, we then expect a mild instability whose form will also be influenced by any further anisotropy, for instance, the usual six-fold one in the (X, Y) plane.
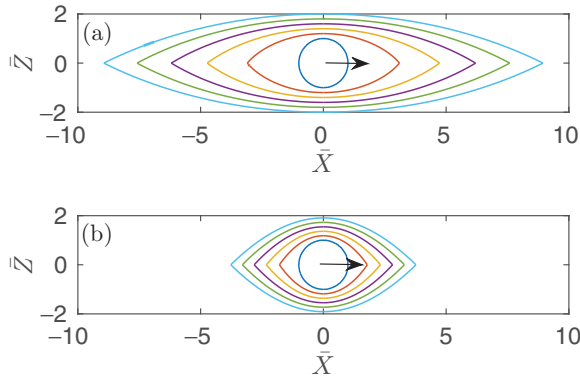
FIGURE 8. Early-time evolutions of an initially spherical melt for anisotropy functions $f(\psi) = \epsilon + \sin^2 \psi$ (panel a) and $f(\psi) = \epsilon/(1 + \epsilon - \sin^2 \psi)$ (panel b), when $\epsilon = 0.1$. The curves in panels (a) and (b) are obtained from the solutions (3.55) and (3.56), respectively. The positions of the interface are shown at equally spaced values of $\bar{s}$ given by $\bar{s} = 0, 2, 4, 6, 8$, and 10, corresponding to rescaled dimensionless times $\bar{\tau} = 0, 2, 2.83, 3.46, 4.0$, and 4.47, respectively. Both anisotropy functions lead to the formation of a corner, and this happens when $\bar{\tau} = 1.49$ in panel (a) and $\bar{\tau} = 0.32$ in panel (b). As $\bar{\tau} \to \infty$, the interface profiles approach the kinetic Wulff shapes shown in Figure 4.

3.4 Other anisotropy functions

We now briefly outline the results that are obtained for the anisotropy functions (2.7) and (2.8). Full details about the solutions in the early-time regime and the solution of Charpit's equations are given in Appendix A.

3.4.1 Dynamics with $f(\psi) = \epsilon + \sin^2 \psi$

In the early-time regime given by $\tau = O(\alpha^{1/2})$, the solid–liquid interface can be written parametrically as

$$X = [\alpha + s(1 + \epsilon + \sin^2 \varphi)] \cos \varphi, \quad Z = [\alpha + s(\epsilon - \cos^2 \varphi)] \sin \varphi, \tag{3.55}$$

where $\varphi \in [0, 2\pi)$ and $s = \tau^2/2$. Interface profiles at various times are shown in Figure 8(a). The interface remains smooth until $s = \tau^2/2 = \alpha/(1 - \epsilon)$, at which point a corner develops at the rim due to intersecting characteristics. The early growth of the rim for $s/\alpha \ll \epsilon$ scales like $S \sim \tau$; however, the longer-term growth of the rim for $s/\alpha \gg \epsilon$ is reduced by the corner and we find that $S \sim \epsilon^{1/2}\tau^2$. The thickness of the melt in the axial direction grows like $\epsilon\tau^2$ for all times.

For larger times, the separation of length scales in the radial and axial directions can, in principle, be exploited and the model can be reduced using a similar analysis to that in Section 3.2. However, the current model is expected to require additional mechanisms such as surface energy to act to regularise the corner. Therefore, we do not proceed with the model reduction in this case. Nevertheless, we note that because of the slower radial growth for early times, in getting to terms to balance in a model equivalent to (3.35), larger time and temperature scalings are needed: $\tau = \epsilon^{-1/4}\tau^*$ and $\theta = \epsilon^{-1/4}\theta^*$.

3.4.2 *Dynamics with $f(\psi) = \epsilon/(1 + \epsilon - \sin^2 \psi)$*

In this case, the position of the interface in the early-time regime, $\tau = O(\alpha^{1/2})$, is given by

$$X = \left[\alpha + \frac{\epsilon s(3\sin^2 \varphi + \epsilon)}{(\sin^2 \varphi + \epsilon)^2}\right] \cos \varphi, \quad Z = \left[\alpha - \frac{\epsilon s(3\cos^2 \varphi - 1 - \epsilon)}{(\sin^2 \varphi + \epsilon)^2}\right] \sin \varphi, \quad (3.56)$$

where, again, $s = \tau^2/2$. Figure 8(b) shows the corresponding interface profiles at various times. Here, the corner appears in the very early stages of melt growth, in particular, when $s = \tau^2/2 = \epsilon\alpha/(2 - \epsilon)$. The growth of the rim scales like $S \sim \alpha + (\alpha\epsilon)^{1/2}\tau$ for $s \ll \alpha/\epsilon$ and like $S \sim \epsilon\tau^2$ for $s \gg \alpha/\epsilon$. The axial growth scales like $\epsilon\tau^2$ for all time.

For this particular anisotropy, the eventual growth of the melt both parallel and normal to the *c*-axis is the same order of magnitude. The aspect ratio of the melt roughly approaches 5:2 and, therefore, it is not possible to simplify the model for $O(1)$ times.

3.4.3 *Commonalities of the early-time growth*

The three anisotropy functions that we consider produce interface profiles with common growth features in the early-time regime. For instance, all three cases lead to melts that evolve into their kinetic Wulff shapes given by (2.6). In fact, an analysis for arbitrary anisotropy functions in Appendix A shows this will always be the case. Furthermore, the growth of the melt in the axial direction, i.e., along the *c*-axis, is always found to be quadratic with time. As shown in Appendix B, if nucleation occurs much later than when the system is irradiated, then the axial growth becomes linear for all anisotropy functions.

4 Discussion and conclusion

In this paper, we have formulated and analysed a mathematical model describing the anisotropic growth of a Tyndall figure into a crystal of superheated ice. Both the solid and liquid phases are assumed to be volumetrically heated by the absorption of incoming radiation, which drives the melting process. The anisotropic growth of the Tyndall figure is a result of the molecularly smoothly basal planes of the ice crystal melting at a much slower rate in comparison to molecularly rough prism planes. This phenomenon is modelled using a kinetic coefficient that depends on the orientation of the solid–liquid interface. The relationship between the kinetic coefficient and the crystal orientation is quantified through an anisotropy function. Our analysis indicates that there are two key time regimes for the melt evolution. The first of these describes the rapid initial growth of the Tyndall figure into its kinetic Wulff shape due to volumetric heating. The second time regime describes the slower, diffusion-dominated growth.

The problem in the first time regime amounted to solving an anisotropic Eikonal equation. Remarkably, it was possible to obtain an analytical solution to this equation for an arbitrary anisotropy functions. Using this solution, we examined the interface profiles and kinetic Wulff shapes that are obtained for three different anisotropy functions. These anisotropy functions led to a rich variety of melt shapes including long rectangles with rounded ends, oblate spheroids, as well as thick and thin lenses. Qualitatively, we found

that the smoothest melts and the smallest aspect ratios occur when the anisotropy function has broad maxima; anisotropy functions with narrow maxima gave rise to corners and lens-shaped melts that can have order-one aspect ratios. Regardless of the anisotropy function, the thickness of the melt in the direction of the *c*-axis was found to grow quadratically with time. This is in contrast to the radial growth parallel to the basal planes, which was highly dependent on the anisotropy function. These findings have important practical implications, as they suggest that experimental data for the radial growth of the melt can aid in the determination of likely candidates for the anisotropy function. This is not the case for axial growth, which is predicted to be roughly the same for all anisotropy functions.

By exploiting the thin aspect ratio of the melt figure, we showed that a simplified model for the evolution in the second time regime can be derived by systematically collapsing the three-dimensional melt figure to a two-dimensional surface with zero thickness along the axial direction. This model was then used to carry out a linear stability analysis, the results of which suggest that an instability will occur if the temperature field locally increases in the direction of radial growth. Such an instability would likely lead to fingers and could drive the formation of a Tyndall star similar to that shown in Figure 1.

The results from our analysis, in combination with the experimental observations by Takeya [29], may give some insight into appropriate anisotropy functions for the melting of ice crystals. In particular, the melts documented by Takeya have a remarkably constant thickness in direction of the *c*-axis which diminishes relatively rapidly near the rim. In addition, the aspect ratio of the melt is small and on the order of 1:10. These observations suggests that an appropriate anisotropy function for modelling the growth of Tyndall figures would be qualitatively like that in (2.5) but with much broader maxima at $\psi = \pm \pi/2$.

Further predictions about Tyndall star evolution can be accessed through numerical simulations of our model. From a computational perspective, simplified models such as (3.35) are advantageous due to the reduced dimensionality of the free boundary and are relatively straightforward to implement. Numerical solutions of such a model can provide insights into when the condition for instability is satisfied and offer a means of probing non-linear melt-figure morphologies. Furthermore, such simulations could explore whether the onset of instability is linked to growth along the *c*-axis, which has been suggested by experimental studies [25, 29]. Thus, there is a wide range of exciting and unanswered problems relating to the formation and evolution of Tyndall stars, and we hope this work not only provides some of the foundations that can aid in tackling these, but also motivation for doing so.

Acknowledgements

References

[1] ANGENENT, S. B. & GURTIN, M. E. (1989) Multiphase thermomechanics with interfacial structure 2. Evolution of an isothermal interface. *Arch. Rat. Mech. Anal.* **108**, 323–391.

[2] ATTHEY, D. R. (1974) A finite difference scheme for melting problems. *IMA J. Appl. Math.* **13**(3), 353–366.

[3] BARLES, G. & SOUGANIDIS, E. (1998) A new approach to front propagation problems: Theory and applications. *Arch. Rat. Mech. Anal.* **141**, 237–296.

[4] BOETTINGER, W. J., WARREN, J. A., BECKERMANN, C. & KARMA A. (2002) Phase-field simulation of solidification. *Ann. Rev. Mater. Res.* **32**, 163–194.

[5] BURTON, W. B., CABRERA, N. & FRANK, F. C. (1951) The growth of crystals and the equilibrium structure of their surfaces. *Philos. Trans. R. Soc. London, Ser. A* **243**(866), 299–358.

[6] CAHOON, A., MARUYAMA, M. & WETTLAUFER, J. S. (2006) Growth-melt asymmetry in crystals and twelve-sided snowflakes. *Phys. Rev. Lett.* **96**, 255502.

[7] CHADAM, J., HOWISON, S. D. & ORTOLEVA, P. (1987) Existence and stability for spherical crystals growing in a supersaturated solution. *IMA J. Appl. Math.* **39**, 1–15.

[8] CORIELL, S. R., MCFADDEN, G. B. & SEKERKA, R. F. (1999) Selection mechanisms for multiple similarity solutions for solidification and melting. *J. Cryst. Growth* **200**, 276–286.

[9] CORIELL, S. R., MCFADDEN, G. B., SEKERKA, R. F. & BOETTINGER, W. J. (1998) Multiple similarity solutions for solidification and melting. *J. Cryst. Growth* **191**, 573–585.

[10] DAVIS, S. H. (2001) *Theory of Solidification*, Cambridge University Press, Cambridge.

[11] FONT, F., MITCHELL, S. L. & MYERS, T. G. One-dimensional solidification of supercooled melts. *Int. J. Heat Mass Tran.* **62**, 411–421.

[12] GURTIN, M. E. (1993) *Thermomechanics of Evolving Phase Boundaries in the Plane,* Clarendon, Oxford.

[13] HU, H. & ARGYROPOULOS S. A. (1996) Mathematical modelling of solidification and melting: A review. *Modelling Simul. Mater. Sci. Eng.* **4**, 371–396.

[14] HARVEY, P. (2013) *An Experimental Analysis of Tyndall Figures*. Technical Report, Department of Earth Science, University of Oxford, Oxford.

[15] HENNESSY, M. G. (2010) *Liquid Snowflake Formation in Superheated Ice*, M.Sc. thesis, University of Oxford, Oxford.

[16] HOWISON, S. D., OCKENDON, J. R. & WILSON, S. K. (1991) Incompressible water-entry problems at small deadrise angles. *J. Fluid Mech.* **222**, 215–230.

[17] HUPPERT, H. E. (1990) The fluid mechanics of solidification. *J. Fluid Mech.* **212**, 209–240.

[18] LACEY, A. A. & HERRAIZ, L. A. (2000) Macroscopic models for melting derived from averaging microscopic Stefan problems I: Simple geometries with kinetic undercooling or surface tension. *Eu. J. Appl. Math.* **11**(2), 153–169.

[19] LACEY, A. A. & HERRAIZ, L. A. (2002) Macroscopic models for melting derived from averaging microscopic Stefan problems II: Effect of varying geometry and composition. *Eu. J. Appl. Math.* **13**(3), 261–282.

[20] LACEY, A. A. & SHILLOR, M. (1983) The existence and stability of regions with superheating in the classical two-phase one-dimensional Stefan problem with heat sources. *IMA J. Appl. Math.* **30**(2), 215–230.

[21] LACEY, A. A. & TAYLER, A. B. (1983) A mushy region in a Stefan problem. *IMA J. Appl. Math.* **30**(3), 303–313.

[22] MAE, S. (1975) Perturbations of disc-shaped internal melting figures in ice. *J. Crystal Growth.* **32**(1), 137–138.

[23] MARUYAMA, M., KURIBAYASHI, N., KAWABATA, K. & WETTLAUFER, J. S. (2000) A test of global kinetic faceting in crystals. *Phys. Rev. Lett.* **85**(12), 2545–2548.

[24] NAKAYA, U. (1956) *Properties of Single Crystals of Ice, Revealed by Internal Melting*, Technical report, Snow Ice and Permafrost Research Establishment, U.S. Army.

[25] MARUYAMA, M. (2011) Relation between growth and melt shapes of ice crystals. *J. Cryst. Growth* **318**, 36–39.

[26] MULLINS, W. W. & SEKERKA, R. F. (1963) Morphological stability of a particle growing by diffusion or heat flow. *J. Appl. Phys.* **34**, 323–329.

[27] OCKENDON, J., HOWISON, S., LACEY, A. & MOVCHAN, A. 2003 *Applied Partial Differential Equations*, Oxford University Press, Oxford.

[28] SHIMADA, W. & FURUKAWA, Y (1997) Pattern formation of ice cystals during free growth in supercooled water. *J. Phys. Chem. B* **101**, 6171–6173.

[29] TAKEYA, S. (2006) Growth of internal melt figures in superheated ice. *Appl. Phys. Lett.* **88**, 074103.

[30] TYNDALL, J. (1858) On some physical properties of ice. *Phil. Trans. Roy. Soc. Lond.* **148**, 211–229.

[31] TSEMEKHMAN, V. & WETTLAUFER, J. S. (2003) Singularities, shocks, and instabilities in interface growth. *St. Appl. Math.* **110**, 221–256.

[32] UEHARA, T. & SEKERKA, R.F. (2003) Phase field simulations of faceted growth for strong anisotropy of kinetic coefficient. *J. Cryst. Growth* **254**, 251–261.

[33] WETTLAUFER, J. S. (2001) Dynamics of ice surfaces. *Interface Sci.* **9**, 117–129.

[34] WETTLAUFER, J. S., JACKSON, M. & ELBAUM, M. (1994) A geometric model for anisotropic crystal growth. *J. Phys. A* **27**, 5957–5967.

[35] YOKOYAMA, E. & KURODA T. (1990) Pattern formation in growth of snow crystals occurring in the surface kinetic process and the diffusion process. *Phys. Rev. A* **41**, 2038–2050.

[36] YOKOYAMA, E. & SEKERKA, R. F. (1992) A numerical study of the combined effects of anisotropic surface tension and interface kinetics on pattern formation during the growth of two-dimensional crystals. *J. Cryst. Growth* **125**, 289–403.

[37] YOKOYAMA, E., SEKERKA, R. F. & FURUKAWA, Y. (2009) Growth of an ice disk: Dependence of critical thickness for disk instability on supercooling of water. *J. Phys. Chem. B* **113**, 4733–4738.

Appendix A solution of Charpit's equations for the anisotropic Eikonal equations

An asymptotic analysis of the model revealed that the early-time interface profiles can be obtained by solving an anisotropic Eikonal equation of the form

$$(s_X^2 + s_Z^2)^{1/2} \hat{f} \left(s_X (s_X^2 + s_Z^2)^{-1/2} \right) = 1, \tag{A 1a}$$

where $s_X = \partial s / \partial X$ and $s_Z = \partial s / \partial Z$. Equation (A 1) is supplemented with the condition

$$s_0 = s(X_0, Z_0) \equiv 0, \quad X_0^2 + Z_0^2 = \alpha^2. \tag{A 1b}$$

The solution to this problem can be obtained using Charpit's equations, which generalise the well-known method of characteristics to fully non-linear first-order hyperbolic partial differential equations (PDEs) [27]. We recall that when applying the method of characteristics, one must simultaneously solve for the characteristic directions and the solution to the PDE on these characteristics. The idea behind Charpit's method is to treat the first derivatives of the solution to the PDE as additional unknowns that must be found along the characteristic directions. Thus, when applying Charpit's method to this problem, we must simultaneously solve for the characteristic directions, X and Z, as well as the solution s and its derivatives s_X and s_Z along the characteristics. Although these five unknowns are effectively treated as independent variables, Charpit's equations ensure that they always vary in a consistent manner.

To apply Charpit's method to equation (A 1), we first let $p = s_X$, $q = s_Z$, and we write the PDE in equation (A 1a) as

$$G(X, Z, s, p, q) = (p^2 + q^2)^{1/2}\hat{f}\left(p(p^2 + q^2)^{-1/2}\right) - 1 \equiv 0. \qquad (A\,2)$$

The condition in equation (A 1b) can be treated as initial data and parametrised according to

$$s_0(\varphi) = s(X_0(\varphi), Z_0(\varphi)) = 0, \quad \zeta = 0, \qquad (A\,3a)$$

$$X_0(\varphi) = \alpha\cos\varphi, \qquad\qquad\qquad \zeta = 0, \qquad (A\,3b)$$

$$Z_0(\varphi) = \alpha\sin\varphi, \qquad\qquad\qquad \zeta = 0, \qquad (A\,3c)$$

where $\varphi \in [0, 2\pi)$ and ζ is an arbitrary parameter that measures distance along each characteristic direction. Initial conditions for p and q, given by p_0 and q_0, can be obtained by (i) differentiating the condition $s_0(\varphi) = s(X_0(\varphi), Z_0(\varphi)) \equiv 0$ with respect to φ and (ii) requiring the PDE equation (A 2) to hold on the initial curve, $G(X_0, Z_0, s_0, p_0, q_0) \equiv 0$. By simultaneously solving two these equations, we obtain

$$p_0(\varphi) = \frac{\cos\varphi}{\hat{f}(\cos\varphi)}, \quad q_0(\varphi) = \frac{\sin\varphi}{\hat{f}(\cos\varphi)}, \quad \zeta = 0. \qquad (A\,3d)$$

Charpit's equations for this problem can be written as

$$\dot{X} = \frac{\partial G}{\partial p}, \qquad (A\,4a)$$

$$\dot{Z} = \frac{\partial G}{\partial q}, \qquad (A\,4b)$$

$$\dot{s} = 1, \qquad (A\,4c)$$

$$\dot{p} = 0, \qquad (A\,4d)$$

$$\dot{q} = 0, \qquad (A\,4e)$$

where the dot denotes differentiation with respect to ζ. Upon solving these equations with the initial conditions in equation (A 3), we find that $s \equiv \zeta$, so that ζ can be replaced by s. In addition, we have $p \equiv p_0$, $q \equiv q_0$, and

$$X = [\alpha + s\hat{f}(\cos\varphi)]\cos\varphi + s\hat{f}'(\cos\varphi)\sin^2\varphi, \qquad (A\,5a)$$

$$Z = [\alpha + s(\hat{f}(\cos\varphi) - \hat{f}'(\cos\varphi))]\sin\varphi \qquad (A\,5b)$$

with the prime denoting derivative with respect to argument.

For the anisotropy function (a) $f(\psi) = (\epsilon^2 + \sin^2\psi)^{1/2}$, we have that $\hat{f}(w) = (\epsilon^2 + w^2)^{1/2}$. After inserting this expression into equation (A 5) and some algebra, the solution can be written as

$$X = \left(\alpha + \frac{s(1 + \epsilon^2)}{(\epsilon^2 + \cos^2\varphi)^{1/2}}\right)\cos\varphi, \quad Z = \left(\alpha + \frac{s\epsilon^2}{(\epsilon^2 + \cos^2\varphi)^{1/2}}\right)\sin\varphi. \qquad (A\,6)$$

The properties of this solution are described in Section 3.1. For the anisotropy functions
(b) $f(\psi) = \epsilon + \sin^2 \psi$ and (c) $f(\psi) = \epsilon/(1 + \epsilon - \sin^2 \psi)$, we find that

$$X = [\alpha + s(1 + \sin^2 \varphi + \epsilon)] \cos \varphi, \quad Z = [\alpha - s(\cos^2 \varphi - \epsilon)] \sin \varphi, \qquad (A\,7)$$

and

$$X = \left[\alpha + \frac{\epsilon s(3 \sin^2 \varphi + \epsilon)}{(\sin^2 \varphi + \epsilon)^2}\right] \cos \varphi, \quad Z = \left[\alpha - \frac{\epsilon s(3 \cos^2 \varphi - 1 - \epsilon)}{(\sin^2 \varphi + \epsilon)^2}\right] \sin \varphi, \qquad (A\,8)$$

respectively. These solutions with $\epsilon = 0.1$ are shown in Figures 5 and 8.

For case (b), focusing on that part of the free boundary lying in the first quadrant,
$0 \leqslant \varphi \leqslant \pi/2$, we see that some of the characteristics are directed down, towards $Z = 0$,
and intersection of characteristics starts, on the X-axis, when $s = \alpha/(1 - \epsilon) \sim \alpha$ at
$X = \alpha + \alpha(1 + \epsilon)/(1 - \epsilon) = 2\alpha/(1 - \epsilon) \sim 2\alpha$. For later times, this method of characteristics
indicates multiple-valued solutions. To avoid this, the convex part of the curve is taken,
giving corners on $Z = 0$ for $s > \alpha/(1 - \epsilon)$. These would be expected to be rounded
off by any sort of surface-tension or surface-energy effects so that a Gibbs–Thomson
term is introduced into the free-boundary conditions. A mathematically simpler way of
regularising the problem would be to replace the anisotropic Eikonal equation, which is
a first-order flow, by a mean-curvature flow. Results of Barles & Souganidis [3] could be
applied to give continuous dependence of solutions on the coefficient of any curvature
term included in (3.5). This would again indicate that we should get the interface by
taking the convex part of the curve.

The same corner formation is seen for the anisotropy function (c). In this case, the
corner forms very quickly, when $s = \epsilon\alpha/(2 - \epsilon)$, and close to the initial free boundary, at
$X = 2\alpha/(2 - \epsilon)$.

The range of possible short-time interface behaviour is large because the growth in the
X direction can have quite different qualitative behaviour. For case (b), with $s \ll \alpha/\epsilon$,
$X = 2s(\epsilon + \alpha/s)^{1/2} \sim 2(\alpha s)^{1/2} = (2\alpha)^{1/2}\tau$ so that the growth is only linear in time. The final
case (c), has $\cos^2 \varphi \sim 1 - (2\epsilon s/\alpha)^{1/2}$ and $X \sim \alpha(1 + (2\epsilon s/\alpha)^{1/2}) = \alpha(1 + (\epsilon/\alpha)^{1/2}\tau)$.

For large times, in the sense of $s \gg \alpha/\epsilon$, the behaviour of Z is the same for all three
anisotropy functions: $Z \sim \epsilon s \sim \epsilon\tau^2/2$. However, the long-time growth in the X direction
is reduced, thanks to the appearance of the corner. For (b), the corner's position is, in
general, given by $X = [\alpha + s(1 + \sin^2 \varphi + \epsilon)] \cos \varphi$ with $Z = [\alpha - s(\cos^2 \varphi - \epsilon)] \sin \varphi = 0$.
Since $0 < \varphi < \pi/2$, this gives $\cos^2 \varphi = \epsilon + \alpha/s$ and $X = 2s(\epsilon + \alpha/s)^{1/2} \sim 2\epsilon^{1/2}s = \epsilon^{1/2}\tau^2$ for
$s \gg \alpha/\epsilon$. Very similar calculations for (c) show that the corner location can be obtained
implicitly from

$$\frac{X}{\alpha} \sim \frac{2\cos \varphi}{3\cos^2 \varphi - 1}, \quad \frac{\epsilon s}{\alpha} \sim \frac{(1 - \cos^2 \varphi)^2}{3\cos^2 \varphi - 1}, \qquad (A\,9)$$

for $0 < \varphi < \cos^{-1}(1/\sqrt{3})$. For $s \gg \alpha/\epsilon$, this gives $\cos^2 \varphi \sim (1/3)$ and we get $X \sim 3^{3/2}/2\epsilon s = (3^{3/2}/4)\epsilon\tau^2$.

By taking the modified time variable s sufficiently large in comparison to α in equation (A 5), the longer-term interface profile for an arbitrary anisotropy function is given by

$$X/s \sim \hat{f}(\cos \varphi) \cos \varphi + \hat{f}'(\cos \varphi) \sin^2 \varphi, \qquad (A\,10a)$$

$$Z/s \sim \hat{f}(\cos \varphi) \sin \varphi - \hat{f}'(\cos \varphi) \cos \varphi \sin \varphi \qquad (A\,10b)$$

independent of the initial shape. Equation (A 10) is, in fact, equivalent to (2.6) and therefore, the interface profiles approach the kinetic Wulff shapes. The direction of the characteristics, Z/X, can be differentiated with respect to φ to check if this ever decreases, leading to corner formation from an initially convex shape. After some manipulation, the derivative turns out to be

$$\left(\hat{f} - \frac{\mathrm{d}}{\mathrm{d}\varphi}(\hat{f}' \sin \varphi) \right) \hat{f} = \left(f + \frac{\mathrm{d}^2 f}{\mathrm{d}\psi^2} \right) f .$$

The criterion for a continued smooth interface is then $f + \mathrm{d}^2 f/\mathrm{d}\psi^2 \geqslant 0$. Cahoon *et al.* [6] and Wettlaufer *et al.* [34] find the same basic law for interface motion gives the rate of change $\mathrm{d}\kappa/\mathrm{d}s = (f + \mathrm{d}^2 f/\mathrm{d}\psi^2)\kappa^2$ for the interface curvature κ. The same key combination appears in curvature-flow models for phase change with significant Gibbs–Thomson effect [1,12]. In these works, the $(f + \mathrm{d}^2 f/\mathrm{d}\psi^2)$ term multiplies curvature in the velocity law and, to avoid negative diffusion, all angles making $(f + \mathrm{d}^2 f/\mathrm{d}\psi^2)$ positive are prohibited, leading to corners in the interface for all positive time.

Appendix B The role of nucleation

We now give a brief discussion of the effect of surface energy in the nucleation process, while still neglecting the air bubble that appears in the melt. We concentrate on the implications of the balance between the superheat temperature and the local equilibrium temperature for a spherical liquid body of a given size; Chadam *et al.* [7] discusses related effects in the growth of crystals when the Gibbs–Thomson effect is the only stabilising action.

We suppose that nucleation occurs when the temperature in the solid exceeds a nucleation temperature T_n given by the Gibbs–Thomson relation

$$T_n = T_0 \left(1 + \frac{2\gamma}{\rho L a_n} \right), \qquad (B\,1)$$

where γ is the interface energy, a_n is the nucleation radius. The time at which nucleation occurs, measured relative to the moment the system is irradiated, is denoted by t_n. Before nucleation occurs, the temperature in the solid increases like $T_s = T_0 + q_s t/(\rho c_{ps})$; therefore, the nucleation time and temperatures can be related via $t_n = \rho c_{ps}(T_n - T_0)/q_s$.

So far we have been assuming that the nucleation temperature is close to the bulk melting temperature, $T_n \simeq T_0$, so that nucleation immediately occurs upon irradiation, resulting in an initial liquid–solid interface that is approximately a sphere of radius a, which is small compared to $\epsilon\ell$. The condition $a \ll \epsilon\ell$ allows the melt to become a developed spheroid when the dimensionless time τ is $O(1)$ in size. Note that if $\epsilon \ll a \ll 1$

there is a significant change to Section 3.2, with the Tyndall figure no longer being of thickness order ϵ.

We now consider the opposite case whereby $T_n \gg T_0$ so that nucleation occurs much later than when the system is first irradiated. The bulk temperatures in this case will be large during the early evolution of the melt and will influence its growth kinetics. To study the behaviour in this late-nucleation regime, we non-dimensionalise (2.1)–(2.3) by writing $\boldsymbol{x} = \bar{\ell}\bar{\boldsymbol{X}}$, $t = t_n + (\bar{\ell}^2/\kappa_s)\bar{\tau}$, and $T = T_0 + \overline{\Delta T}\bar{\theta}$, where $\overline{\Delta T} = T_n - T_0 = 2\gamma/(\rho L a_n)$ and $\bar{\ell} = k_s/(\rho c_{ps}\overline{\Delta T}K)$. The dimensionless volumetric heat sources given by $q_i\bar{\ell}^2/(\rho c_{ps}\overline{\Delta T})$ characterise the temperature rises that occur on the diffusive time scale due to absorption relative to the nucleation temperature $\overline{\Delta T} = T_n - T_0$. These relative temperature rises are expected to be small so the volumetric source terms are neglected from the model, i.e., we take $q_i\bar{\ell}^2/(\rho c_{ps}\overline{\Delta T}) \simeq 0$. The dimensionless bulk equations for the temperatures can be written as

$$\frac{\partial \bar{\theta}_s}{\partial \bar{\tau}} = \nabla^2 \bar{\theta}_s, \quad \bar{\boldsymbol{X}} \in \bar{\Omega}_s(\bar{\tau}), \tag{B 2a}$$

$$\hat{c}_p \frac{\partial \bar{\theta}_l}{\partial \bar{\tau}} = \hat{k}\nabla^2 \bar{\theta}_l, \quad \bar{\boldsymbol{X}} \in \bar{\Omega}_l(\bar{\tau}), \tag{B 2b}$$

which have initial conditions $\bar{\theta}_s = \bar{\theta}_l = 1$ when $\bar{\tau} = 0$ and far-field conditions $\bar{\theta}_s \sim 1$ for $|\bar{\boldsymbol{X}}| \to \infty$. At the free boundary, the Stefan condition reads

$$\bar{v} = \bar{\beta}^{-1}\left(\frac{\partial \theta_s}{\partial n} - \hat{k}\frac{\partial \theta_l}{\partial n}\right), \quad \bar{\boldsymbol{X}} \in \bar{\Gamma}(\bar{\tau}), \tag{B 2c}$$

where the Stefan number is now given by $\bar{\beta} = L/(c_{ps}\overline{\Delta T})$. The anisotropic kinetic condition is

$$\bar{v} = \bar{\theta}_l f(\psi), \quad \bar{\boldsymbol{X}} \in \bar{\Gamma}(\bar{\tau}). \tag{B 2d}$$

The initial interface $\bar{\Gamma}(0)$ is assumed to be a circle of dimensionless radius $\bar{\alpha} = a_n/\bar{\ell}$.

In order to obtain the same asymptotic regimes as in the early-nucleation case considered in the main text, we let $\bar{\beta}^{-1} = \bar{b}\epsilon$ and require the dimensionless initial melt radius to satisfy $\bar{\alpha} \ll \epsilon$. The condition $T_n \gg T_0$ imposes an additional restriction on the dimensionless nucleation radius given by $\bar{\alpha} \ll 2\gamma/(\rho L\bar{\ell})$. Thus, in dimensional terms, we require

$$a_n \ll \min\left\{\epsilon\bar{\ell},\ \frac{2\gamma}{\rho L}\right\}. \tag{B 3}$$

We now summarise the early-time, $\bar{\tau} \ll \bar{\alpha}$, and order-one time, $\bar{\tau} = O(1)$, problems in the late-nucleating regime.

The early-time problem valid for $\bar{\tau} \ll \bar{\alpha}$ can be deduced by repeating the analysis of Section 3.1. The lack of a volumetric heat source means that the leading-order temperatures (in $\bar{\alpha}$) are constant in time, $\bar{\theta}_l = \bar{\theta}_s \equiv 1$. Thus, the anisotropic kinetic condition becomes $\bar{v} = f(\psi)$, which is now autonomous in the time variable $\bar{\tau}$. As a consequence, the growth kinetics of the melt are modified. For the anisotropy function given by

$f(\psi) = (\epsilon^2 + \sin^2 \psi)^{1/2}$, we find that the interface can be written parametrically as

$$\bar{X} = \left[\bar{\alpha} + \frac{\bar{\tau}(1 + \epsilon^2)}{(\epsilon^2 + \cos^2 \varphi)^{1/2}}\right] \cos \varphi, \quad \bar{Z} = \left[\bar{\alpha} + \frac{\bar{\tau}\epsilon^2}{(\epsilon^2 + \cos^2 \varphi)^{1/2}}\right] \sin \varphi, \quad \text{(B 4)}$$

where $\varphi \in [0, 2\pi)$. Thus, the thickness and rim of the melt now grow linearly with time rather than quadratically. However, the morphological characteristics of the interface remain the same as in the early-nucleation regime and, in particular, the kinetic Wulff shapes are still approached in the longer term. Similar changes are seen for other anisotropy functions as well; that is, the powers of τ in the growth laws are reduced by a factor of two.

For $O(1)$ times and the anisotropy function $f = (\epsilon^2 + \sin^2 \psi)^{1/2}$, the analysis in Section 3.2 can also be repeated in order to derive a simplified model that collapses the melt region onto the $\bar{Z} = 0$ axis. In particular, the temperature in the solid satisfies the equation

$$\frac{\partial \bar{\theta}_s}{\partial \bar{\tau}} = \nabla^2 \bar{\theta}_s, \quad \bar{Z} > 0 \qquad \text{(B 5}a)$$

with $\bar{\theta}_s = 1$ when $\bar{\tau} = 0$ and $\bar{\theta}_s \sim 1$ as $|\mathbf{X}| \to \infty$. The boundary conditions on $\bar{Z} = 0$ are given by

$$\frac{\partial \bar{h}}{\partial \bar{\tau}} = \bar{b} \frac{\partial \bar{\theta}_s}{\partial \bar{Z}}, \qquad\qquad \bar{Z} = 0, \ \bar{R} < \bar{S}(\bar{\tau}), \qquad \text{(B 5}b)$$

$$\frac{\partial \bar{h}}{\partial \bar{\tau}} = \bar{\theta}_s \left[1 + \left(\frac{\partial \bar{h}}{\partial \bar{R}}\right)^2\right]^{1/2}, \quad \bar{Z} = 0, \ \bar{R} < \bar{S}(\bar{\tau}), \qquad \text{(B 5}c)$$

$$\frac{\partial \bar{S}}{\partial \bar{\tau}} = \bar{\theta}_s, \qquad\qquad \bar{Z} = 0, \ \bar{R} = \bar{S}(\bar{\tau}), \qquad \text{(B 5}d)$$

$$\frac{\partial \bar{\theta}_s}{\partial \bar{Z}} = 0, \qquad\qquad \bar{Z} = 0, \ \bar{R} > \bar{S}(\bar{\tau}). \qquad \text{(B 5}e)$$

Finally, we require that

$$\bar{h}(\bar{S}(\bar{\tau}), 0, \bar{\tau}) = 0. \qquad \text{(B 5}f)$$